Journal of Nuclear Materials 541 (2020) 152336

Contents lists available at ScienceDirect

Journal of Nuclear Materials

journal homepage: www.elsevier.com/locate/jnucmat

A novel displacement cascade driven irradiation creep mechanism in α-zirconium: A molecular dynamics study

Nargisse Khiara [a, e], Fabien Onimus [a, *], Laurent Dupuy [a], Wassim Kassem [a], Jean-Paul Crocombette [b], Thomas Pardoen [c], Jean-Pierre Raskin [d], Yves Bréchet [e]

[a] Université Paris-Saclay, CEA, Service de Recherches Métallurgiques Appliquées, 91191, Gif-sur-Yvette, France
[b] Université Paris-Saclay, CEA, Service de Recherches de Métallurgie Physique, 91191, Gif-sur-Yvette, France
[c] Institute of Mechanics, Materials and Civil Engineering, Université catholique de Louvain, Place Sainte Barbe 2 L5.02.02, 1348, Louvain-la-Neuve, Belgium
[d] Institute of Information and Communication Technologies, Electronics and Applied Mathematics, Université catholique de Louvain, Place du Levant 2 L5.04.04, 1348, Louvain-la-Neuve, Belgium
[e] Science et Ingénierie des Matériaux et Procédés (SIMAP), Université Grenoble Alpes, 1130 rue de la Piscine BP 75, 38402, Saint Martin d'Hères, France

GRAPHICAL ABSTRACT

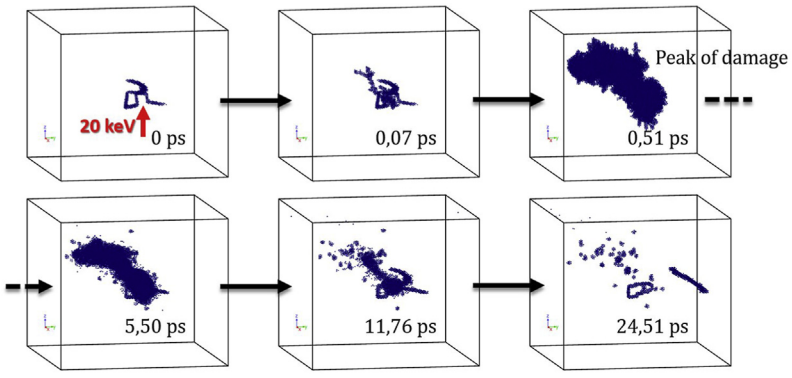

ARTICLE INFO

Article history:
Received 7 February 2020
Received in revised form
7 May 2020
Accepted 16 June 2020
Available online 19 July 2020

Keywords:
Irradiation
Creep
Zirconium
Molecular dynamics

ABSTRACT

Zirconium alloys used in nuclear reactors undergo irradiation creep, which consists of a visco-plastic deformation activated by irradiation occurring under constant load. However, the fundamental underlying mechanisms have not been unraveled yet. A new high-stress irradiation creep mechanism for recrystallized Zircaloy-4 has recently been proposed based on in situ ion irradiation deformation experiments. A displacement cascade is assumed to induce a direct unpinning of a dislocation from an irradiation defect if the cascade occurs within an effective volume around the pinning point. In the present work, a systematic molecular dynamics study was performed to investigate the effect of a 20 keV cascade occurring near <a>-screw dislocation pinned on an interstitial <a>-loop. The direct release of dislocations by displacement cascades is predicted by the simulations. This release is more likely around the pinning points and with increasing stress, in agreement with experimental observations. The effective volume is roughly estimated for three stress levels equal to $0.89\tau_c$, $0.93\tau_c$ and $0.97\tau_c$, with τ_c

* Corresponding author.
E-mail addresses: Nargisse.KHIARA@cea.fr (N. Khiara), Fabien.ONIMUS@cea.fr (F. Onimus), laurent.dupuy@cea.fr (L. Dupuy), Wassim.KASSEM@cea.fr (W. Kassem), Jean-Paul.CROCOMBETTE@cea.fr (J.-P. Crocombette), thomas.pardoen@uclouvain.be (T. Pardoen), jean-pierre.raskin@uclouvain.be (J.-P. Raskin), yves.brechet@grenoble-inp.fr (Y. Bréchet).

https://doi.org/10.1016/j.jnucmat.2020.152336

being the critical stress for unpinning (without irradiation). A mechanism is proposed suggesting that unpinning occurs when the displacement cascade encompasses, at its peak of damage, the two pinning points of the dislocation. A methodology requiring acceptable computation time has been implemented to estimate the effective volume for various cascade energies and loop characteristics, faithfully reproducing the MD results. The mean pinning lifetime calculated using the model provides values of the same order of magnitudes as in the in situ deformation experiments under ion irradiation at high stress levels.

1. Introduction

Zirconium alloys are used in Pressurized Water Reactor (PWR) as claddings and structural materials for the low thermal neutron absorption cross section, good corrosion resistance, high melting point and adequate mechanical properties [1]. However, these claddings are subjected to fast neutron fluxes, high stresses and high temperatures, which lead to significant microstructure changes and macroscopic deformations [2]. The two main irradiation-induced macroscopic deformation modes are irradiation creep and stress-free growth [2–7].

Irradiation creep, which consists of a visco-plastic deformation occurring at temperatures below $0.3T_m$ under constant load and activated by irradiation, has been widely investigated ever since it was observed in the first nuclear reactors [8–10]. The creep parameters and their dependence on neutron flux and fluence, temperature, stress and material variables have been measured using in-reactor uniaxial or biaxial creep, shear (with helical springs) and stress-relaxation using bending tests [4,11,12]. Many theoretical mechanisms have been proposed for this phenomenon [6,13–16], all involving atomic displacements and creation of vacancies and interstitials under fast neutron irradiation, but differing in the fate of the point defects: (1) preferred absorption of point defects by dislocations depending on the orientation of the applied stress also called Stress-Induced Preferential Absorption (SIPA); (2) preferred nucleation of interstitial loops also called Stress-Induced Preferential loop Nucleation (SIPN); (3) unfaulting of interstitial loops; (4) climb-enhanced glide; (5) enhanced recovery mechanisms; (6) internal-stress-driven creep due to irradiation growth. However, there is very few experimental evidence and thus limited basis to assess the relevant controlling mechanisms [17].

Very recently, Gaumé et al. [18] performed in situ ion irradiation (1 MeV Kr^+, flux 6.10^{14} ions/m^2/s, final fluence ranged between $1-3.10^{18}$ ions/m^2) on recrystallized Zircaloy-4 under controlled displacement mode inside a transmission electron microscope (TEM). The experiments were performed at room temperature and at higher temperatures, in the range between 350 °C and 450 °C. Displacement on the tensile specimen was applied until the detection of the first dislocation movements. The applied displacement was then stopped with the load progressively relaxing due to overall dislocation motion. The experiments were thus performed at high stress levels just below the critical stress for dislocation motion. Then, periods of few tens of seconds with and without irradiation were imposed. After the dislocations were first pinned on irradiation-induced point defects, a stop-and-go dislocation motion was observed: when the ion beam was off, the dislocations were pinned on irradiation-induced defects, and once the ion beam was switched on, if the stress level was high enough, the dislocations started to glide, thus bypassing the irradiation defects. Based on these observations, Gaumé et al. [18] proposed a new high-stress irradiation creep mechanism for zirconium alloys. The displacement cascades are assumed to induce directly the unpinning of dislocations locked on irradiation-induced point defects clusters. A dislocation unpins when a cascade occurs within an effective volume (V_{eff}) around its pinning point. Based on several dislocation motion observations, the lifetime (t_w) of the pinning points was estimated to be around 25 s at room temperature and 6 s at 380 °C. Kelly and Foreman [19] proposed a similar pinning-unpinning model under irradiation for graphite.

Previous simulation studies of displacement cascades in α-zirconium, especially with Molecular Dynamics (MD), mainly focused on the creation of irradiation-induced defects [20,21]. The effects of temperature [22,23], strain [24], and the presence of an edge dislocation [25] on the creation of irradiation defects by displacement cascades have been investigated. Furthermore, numerous MD studies have been carried out to study dislocation interaction with irradiation-induced point defects in α-zirconium [26–28]. Serra et al. [27] used MD to simulate the interaction between $1/3<11\bar{2}0>\{1\bar{1}00\}$ dislocations and $1/3<11\bar{2}0>$ interstitial loops. The authors showed that the obstacle resistance is stronger for screw dislocations in comparison with edge dislocations, the strongest configuration corresponding to a loop and a screw dislocation interacting to form a helical turn. For instance, when the Burgers vectors of the screw dislocation and the loop are parallel, the formation of a helical turn occurs if the loop intercepts the glide plane of the dislocation. Regardless of the configuration that induces the formation of the helical turn, the critical stress, which is the stress level necessary for the release of the dislocation, remains the same.

To our knowledge, no MD study about the impact of displacement cascades on dislocation interactions with irradiation defects has been performed up to now. In this work, we investigate, with MD, the cascade-induced unpinning of a $1/3<11\bar{2}0>\{1\bar{1}00\}$ screw dislocation forming a helical turn with an $1/3<11\bar{2}0>\{1\bar{1}00\}$ interstitial loop. The objective is to unravel the necessary conditions to trigger the dislocation unpinning by displacement cascades. In order to reach this objective, the effects of the primary-knock-on atom (PKA) position and of the stress level on the unpinning are systematically studied and the effective volume around the pinning point is estimated (section III). A new irradiation creep model is then proposed based on these MD calculations (section IV) and the results are compared to Gaumé et al. [18] experimental observations in terms of mean pinning lifetime (section V).

2. MD simulation method

2.1. Interaction dislocation/loop

All the simulations were performed using the LAMMPS code [29]. The embedded atom method (EAM) potential #3 for HCP-Zr developed by Mendelev and Ackland [30] was used to describe the interatomic interactions. Previous studies have shown that this potential provides a realistic description of stacking fault energies and dislocation properties [27,31,32], and of primary collision cascades [25,33].

The dimensions of the Zr-crystal simulation box are equal to $112a \times 64c \times 48a\sqrt{3}$. The MD box contains thus approximatively 1 376 400 atoms. As shown in Fig. 1a, the X, Y and Z directions correspond to the HCP crystal axes $[11\bar{2}0]$, $[0001]$, $[\bar{1}100]$. Periodic boundary conditions were applied in the X direction and Y direction.

A perfect crystal is first generated with the selected orientation. A screw dislocation with a Burgers vector $\boldsymbol{b} = a/3 < 11\bar{2}0 >$ is introduced into the MD box using the periodic array of dislocations model (PAD) [34,35]. After relaxation of the system, atoms are added in interstitial positions following a rectangular pattern to generate an interstitial loop containing 144 SIAs. A rectangular shaped loop instead of a more realistic circular loop is chosen in order to reproduce the same configuration as in Ref. [27]. The dimensions are approximately equal to 3.1 nm × 3.4 nm, with the center of the loop lying on the dislocation glide plane. As mentioned before, if the screw dislocation and the loop have the same Burgers vector, the strongest obstacle (helical turn) is formed when the loop intercepts the glide plane of the dislocation.

As in Ref. [27], the crystal, containing both a screw dislocation and an interstitial dislocation loop, is first thermally equilibrated at 300 K for 50 ps with a time-step of 5 fs. The crystal is divided into three layers along the Z-direction. In the top and bottom layers (each one corresponding to $2.5a\sqrt{3}$), the atoms are held in fixed positions with respect to each other. No constraint is imposed to the atoms of the middle layer. In order to induce the glide of the dislocation, a shear strain ε_{xy} corresponding to a strain rate of 10^7 s^{-1} is applied to the atoms of the top layer while the atoms of the bottom layer are held fixed. The corresponding shear stress is calculated using Eq. (1), where F_x is the force applied by the free atoms of the middle layer on the atoms of the upper layer:

$$\tau = \frac{F_x}{L_x L_y} \tag{1}$$

The critical (or unpinning) stress τ_c is taken to be the shear stress necessary for the release of the dislocation without cascade.

The post-processing is performed using the processing and visualization software OVITO [36]. The common neighbor analysis method (CNA [37]) is used to display the atoms not in ideal HCP lattice structure and the dislocation extraction algorithm (DXA [38]) is used to identify the dislocation defects. These methods are both implemented in OVITO [36].

As described by Serra and Bacon [27], during the interaction of the screw dislocation with the interstitial loop, a left-handed helical turn is formed when the dislocation absorbs the loop. As the stress increases, the helical turn first expands to reduce its energy and then shortens until it closes for a critical stress at 300 K $\tau_c = 230$ MPa. The dislocation is thus released and resumes its glide. Yet as shown in Fig. 2, in our MD simulations, we observed a phenomenon that was not explicitly described in Ref. [27]. Before the helical turn shortening, one of the basal segments cross slips to the prismatic plane and then lengthens under increasing stress. Its endpoints, referred to in the following as the pinning points of the dislocation (represented by two orange points in Fig. 2) come closer and finally meet to form the new released screw dislocation.

2.2. Cascade effect on pinned dislocation

The atomic positions corresponding to different large strain levels (and thus high stress levels) prior to the unpinning are first extracted to carry out MD calculations of cascades on these new configurations. The stress levels investigated in this study are $0.86\tau_c$, $0.89\tau_c$, $0.93\tau_c$ and $0.97\tau_c$. The atoms of the top and bottom layers along the Z-direction are fixed: the total strain is held constant (each strain level corresponding to one of the chosen stress levels), as shown in Fig. 1b. The crystal is first thermally equilibrated at 300 K for 50 ps with a time step of 5 fs. Then, the cascade is generated by transferring an energy of 20 keV to a chosen atom (PKA). The corresponding velocity is always applied along the Z-direction $[\bar{1}100]$. This direction is chosen both because it is not a dense direction of the HCP crystal and for practical reasons since there is only a translation over the Z axis (with a magnitude depending on the cascade energy) between the PKA position and the cascade center. The different PKA positions selected for each stress level will be detailed in sections 3.1 and 3.2. A variable time step is set so that the limit in distance travelled by the atoms is less than 1% of the lattice constant. The simulations are run for 150 000 time steps, which represents approximately 100 ps.

3. MD simulation results

3.1. Impact of the PKA position

In order to investigate the impact of the PKA position, a grid (represented in Fig. 3) of 60 Å × 50 Å × 40 Å with a mesh size of

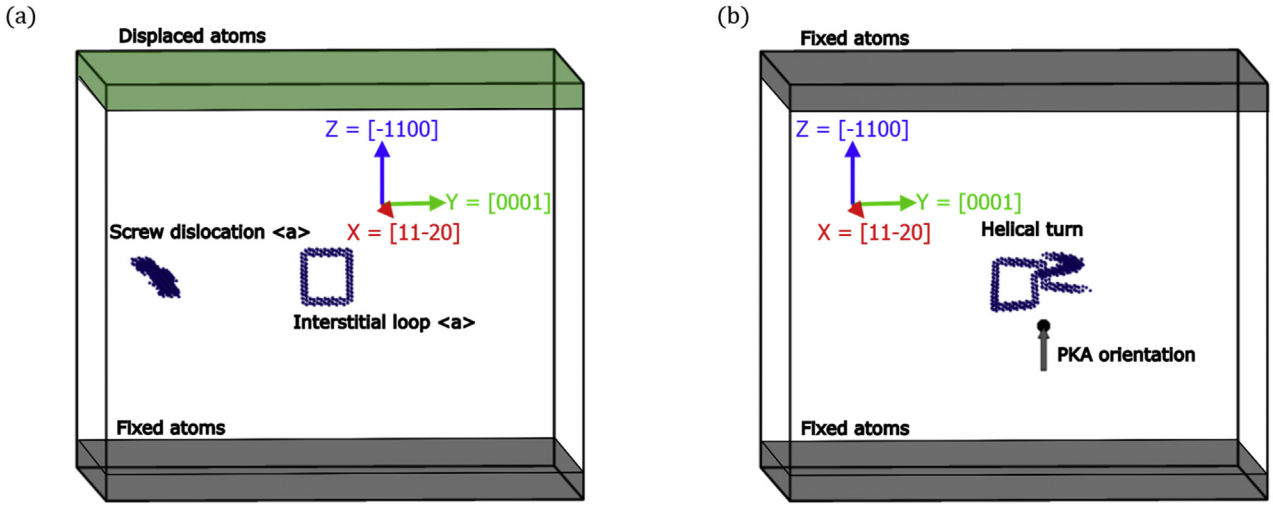

Fig. 1. Boundary conditions (using the CNA method): (a) for the interaction of the dislocation with the loop – (b) for the cascade calculations.

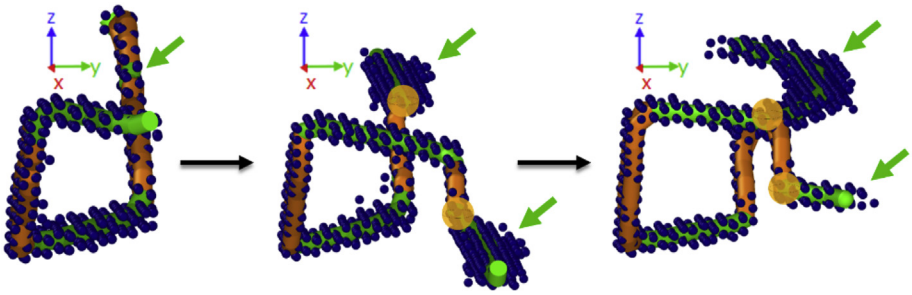

Fig. 2. Snapshots showing the time evolution of the core atoms (using the CNA method) of the screw dislocation and interstitial loop during their interaction; the green arrows point toward the cross-slipped segments, and the large orange points represent the endpoints of this segment; the dislocation segments are displayed according to their type: the green and the orange segments are respectively in the prismatic and basal planes. (For interpretation of the references to color in this figure legend, the reader is referred to the Web version of this article.)

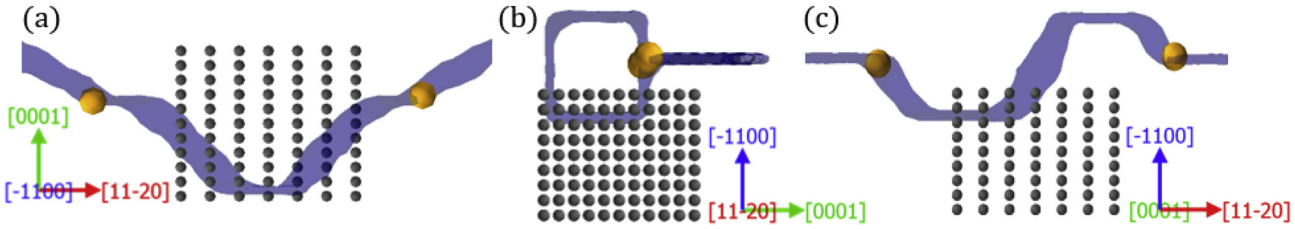

Fig. 3. Grid of PKAs investigated for a stress level of $0.86\tau_c$: the dislocation pinned on the loop is represented in blue, the two large orange dots represent the pinning points of the dislocation, and the small grey dots represent the investigated PKAs. (For interpretation of the references to color in this figure legend, the reader is referred to the Web version of this article.)

10 Å × 5 Å × 5 Å is defined around the helical turn for a stress level of $0.86\tau_c$. As a result, 693 PKA positions can be investigated. This grid lies under the dislocation glide plane since every PKA is given a velocity along + *Z*-axis ($[\bar{1}100]$), and therefore generates a displacement cascade above it.

In the following, the PKAs that induced and did not induce the unpinning of the dislocation are respectively referred to as "efficient" and "inefficient" PKAs.

Fig. 4 shows the evolution of a dislocation pinned on a loop in a case where the unpinning was triggered by the displacement cascade. Although it is not clear what happens at the cascade peak of damage, it appears that, the PKA is "efficient" when the cascade is generated around the helical turn, encompassing the pinning points of the dislocation. The dislocation is then released due to the reorganization of atoms during the cascade relaxation. Furthermore, in most cases, the residual loop is partially destructed by the cascade. After the relaxation of the cascade, it is distorted and its size is reduced by around 50% of its initial area. The interstitials, in excess, are distributed over several small clusters around the residual loop. As represented in Fig. 5, in the cases where the PKA is "inefficient", the pinning points of the dislocation are not entirely encompassed by the cascade at its damage peak, suggesting that the unpinning occurs when the cascade covers both pinning points of the dislocation.

Supplementary video related to this article can be found at https://doi.org/10.1016/j.jnucmat.2020.152336

Fig. 6 shows the results of the simulations in the form of histograms for the unpinning probability as a function of position of the PKA for the *X*-axis $[11\bar{2}0]$, *Y*-axis [0001], and *Z*-axis $[\bar{1}100]$. Over the *X*-axis (Fig. 6a), the unpinning is more often observed when the PKAs occur at around half-way between the two pinning points of the dislocation (represented by the two large yellow dots). The "efficient" PKAs are preferentially located over the *Y*-axis near the two pinning points (Fig. 6b). Over the *Z*-axis (Fig. 6c), the unpinning is more likely for a PKA located 3–5 nm below the dislocation glide plane. These results suggest again that the unpinning occurs when the cascade covers up both pinning points of the dislocation, as depicted in Fig. 4. Nevertheless, the unpinning activation keeps an intrinsic probabilistic nature, supposedly due to the random choice, in MD calculations, of initial atomic positions and velocities around the equilibrium, which induces heterogeneities in the shape of the cascade. This highlights, once again, that the unpinning activation heavily depends on the shape and position of the cascade with respect to the pinning points.

3.2. Impact of the applied stress level

Calculations are performed for three strain levels (prior to the unpinning) corresponding to stresses of approximatively $0.89\tau_c$, $0.93\tau_c$ and $0.97\tau_c$. Two mesh levels are defined: a coarse mesh of 120 Å × 160 Å × 120 Å with a mesh size of 40 Å (80 PKA positions) and a refined mesh of 30 Å × 30 Å × 30 Å with a mesh size of 10 Å (64 PKA positions). The results are represented in Fig. 7. They show that the number and spatial extent of the "efficient" PKAs increase with the magnitude of the stress.

One of the key parameters defined by Gaumé et al. [18] is the effective volume around the pinning points, which is the fictitious volume in which the unpinning is always activated if the PKA is located inside. Considering that the meshed volume V_{mesh} in the case of the coarse mesh is large enough to contain all the possible "efficient" PKAs, one can roughly estimate this effective volume from the total unpinning probability *P* in the meshed volume: $V_{\text{eff}} = P \times V_{\text{mesh}}$. The effective volume is independent of the volume V_{mesh}. The results at the three stress levels investigated using the coarse mesh ($0.89\tau_c$, $0.93\tau_c$ and $0.97\tau_c$) are presented in Table 1. The effective volume increases with the stress, which is consistent with the fact that as the stress increases, the two pinning points come closer and are more likely to be encompassed within the cascade.

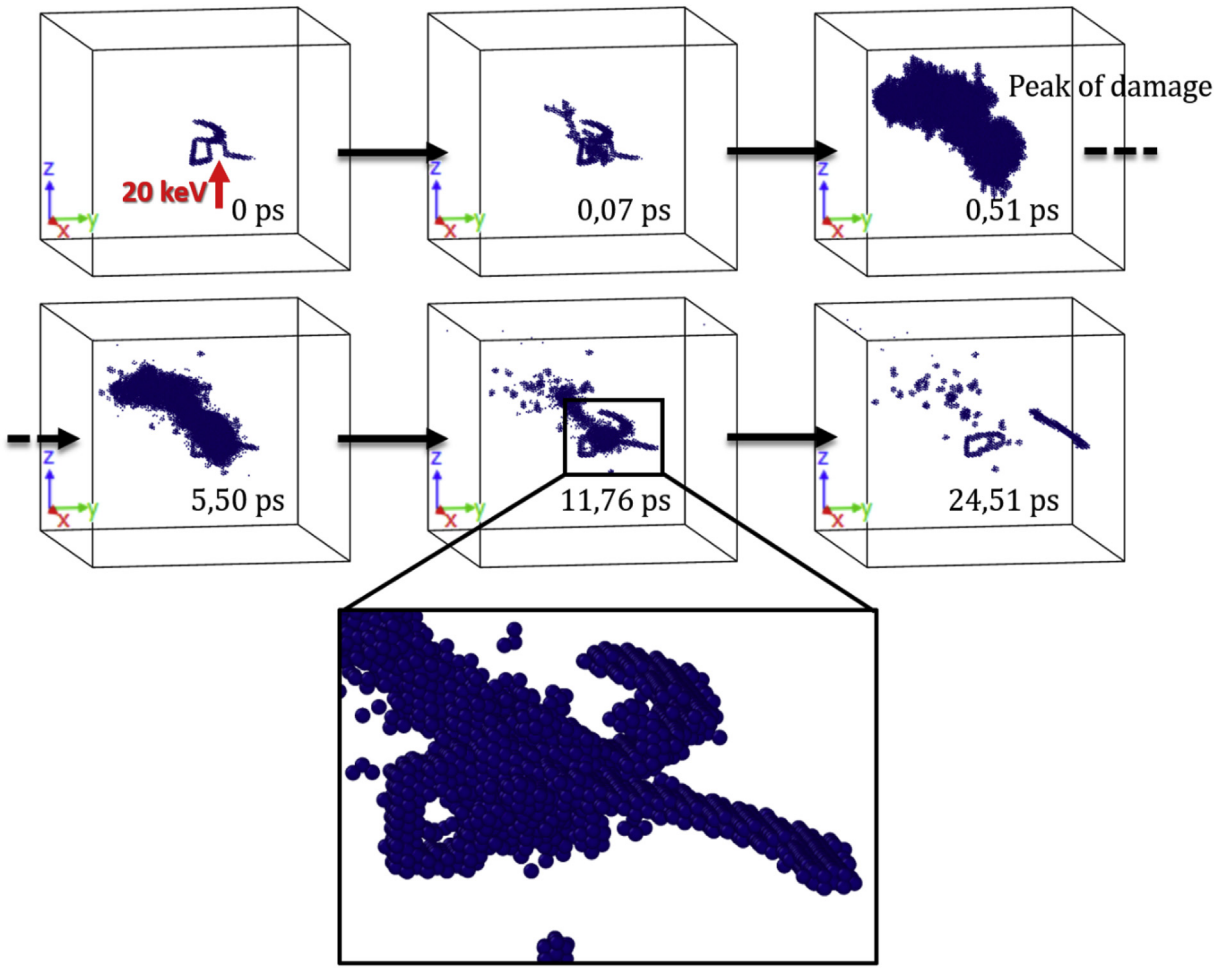

Fig. 4. Snapshots showing time evolution of core atoms (using the CNA method) in a case where the unpinning of the dislocation is triggered (the video can be found in the Supplementary data).

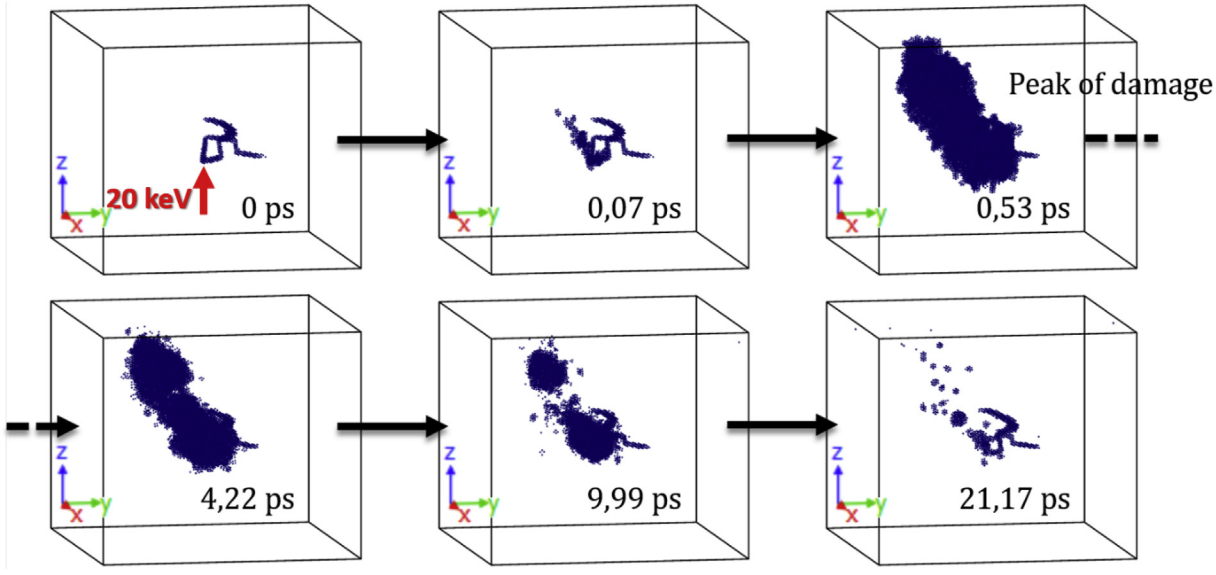

Fig. 5. Snapshots showing time evolution of core atoms (using the CNA method) in a case where the unpinning of the dislocation is not activated (the video can be found in the Supplementary data).

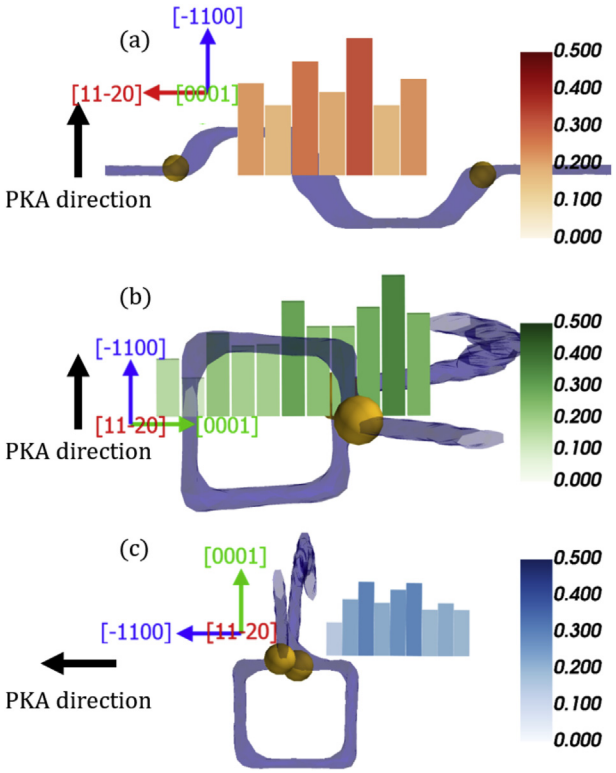

Fig. 6. Histograms of the unpinning probability as a function of the position of the PKA: (a) along the *X*-axis [11$\bar{2}$0]; (b) along the *Y*-axis [0001]; (c) along the *Z*-axis [$\bar{1}$100].

The MD calculations have indicated that, for cascades resulting from a 20 keV energy PKA, the unpinning of the dislocation can occur and is more likely when the cascade covers both pinning points of the dislocation. Moreover, the effective volume increases with the stress, most probably resulting from the fact that the two pinning points come closer together with increasing stress.

Table 1
Effective volumes estimated with the coarse mesh for cascades resulting from a 20 keV energy PKA.

Stress (MPa)	Effective volume V_{eff} (nm^3)
$0.89\tau_c$	136.9 nm^3
$0.93\tau_c$	205.3 nm^3
$0.97\tau_c$	775.6 nm^3

4. Closed-form model

4.1. Unpinning mechanism

The model developed to calculate the effective volume, without having to perform a statistical study of the possible unpinning of a dislocation by a cascade using molecular dynamics, is based on the assumption that for the unpinning to occur, the cascade must encompass both pinning points of the dislocation. If a cascade is considered spherical, as shown in Fig. 8, and given the symmetry of the problem, the effective volume corresponds then to the intersection of two spheres having a radius equal to the cascade radius R_c and having the centers separated by a distance $\Delta^{\text{loop}}(\tau)$, which is the distance between the two pinning points. This distance depends on the characteristics of the loop microstructure (dimensions and box size), and, as mentioned earlier, it decreases with the stress. Even though the cascades are not strictly spherical, we consider that, on average, due to the random orientation of the cascade, they can be approximated by a sphere with radius R_c.

Under this hypothesis, for a given loop and a PKA energy E_{PKA}, the effective volume $V_{\text{eff}}^{\text{loop}}$ can be calculated as follows:

If $R_c < \frac{\Delta^{\text{loop}}(\tau)}{2}$, then:

$$V_{\text{eff}}^{\text{loop}}(\tau, E_{\text{PKA}}) = 0\,. \tag{2}$$

If $R_c \geq \frac{\Delta^{\text{loop}}(\tau)}{2}$, then:

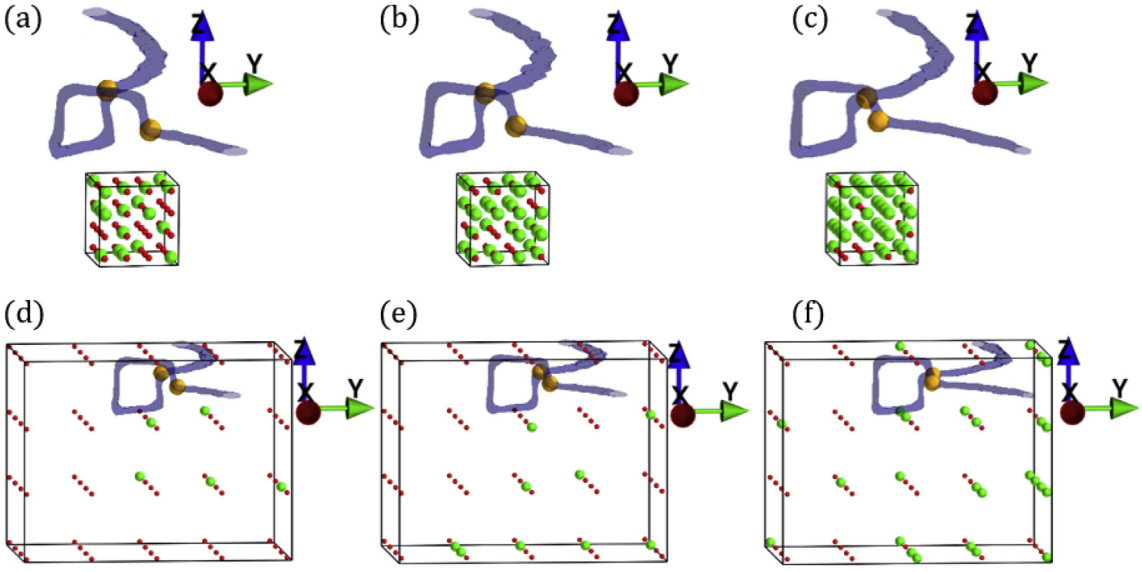

Fig. 7. MD simulations at 3 stress levels: (a) and (d), (b) and (e), (c) and (f) represent the dislocation and the results for the refined and the coarse mesh for stress levels of respectively $0.89\tau_c$, $0.93\tau_c$ and $0.97\tau_c$), the helical turn is represented in blue, the large green dots represent the "efficient" PKAs and the small red dots represent the "inefficient" PKAs. (For interpretation of the references to color in this figure legend, the reader is referred to the Web version of this article.)

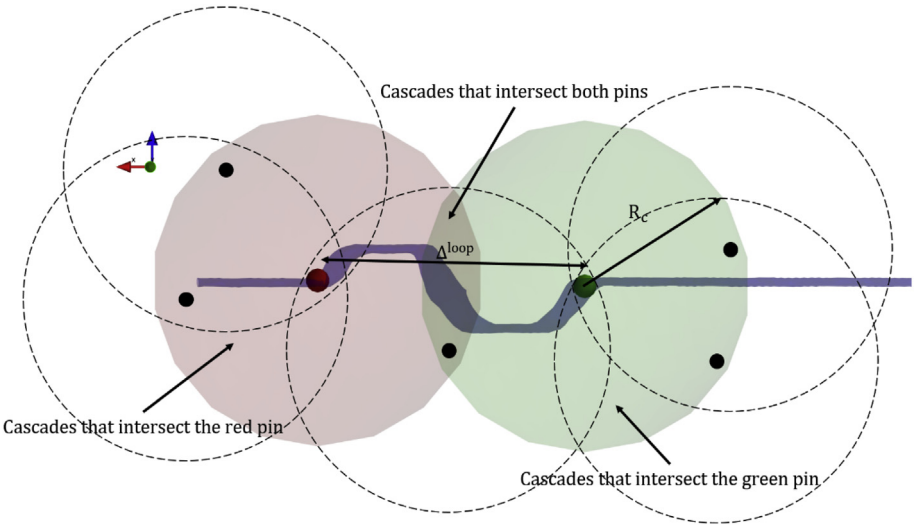

Fig. 8. Display of the "efficient" cascades in the proposed mechanism: the red and green points represent the two pinning points of the dislocation. The red and green spheres represent the centers of the cascades that intersects each pinning point, the "efficient" cascades lie in the intersection of both spheres, small black dots and black dotted lines represent possible cascades centers and extension. (For interpretation of the references to color in this figure legend, the reader is referred to the Web version of this article.)

$$V_{eff}^{loop}(\tau, E_{PKA}) = \frac{\pi}{12}\left(4R_c(E_{PKA}) + \triangle^{loop}(\tau)\right)\left(2R_c(E_{PKA})\triangle^{loop}(\tau)\right)^2 \quad (3)$$

.

Therefore, the determination of the effective volume is reduced to purely geometrical considerations that require the calculations of only two parameters: the cascade radius, $R_c(E_{PKA})$ and the distance between the two pinning points, $\Delta^{loop}(\tau)$.

4.2. Determination of the distance $\Delta^{loop}(\tau)$

As mentioned before, during the interaction between the dislocation and the loop, one of the basal segments needs to cross-slip to the prismatic plane to form the new screw dislocation segment (and create pinning points). Since a high stress mechanism is addressed, we only consider here stress levels above $0.6\tau_c$.

The pinning points come closer with increasing stress (Fig. 7). In order to determine the pinning points spacing $\Delta^{loop}(\tau)$, the dislocation is extracted using the DXA module at each time-step of a MD simulation dealing with the interaction of a dislocation with a loop without cascade. The distance $\Delta^{loop}(\tau)$ between the two pinning points is monitored. Fig. 9 represents the decrease of Δ^{loop} with increasing stress.

4.3. Determination of the cascade radius $R_c(E_{PKA})$

4.3.1. Estimate of the cascade radius

Given $\Delta^{loop}(\tau)$ and using Eq. (3), the effective volume can be estimated for several test cascade radii for the three stress levels investigated in the previous MD simulations ($0.89\tau_c$, $0.93\tau_c$, and $0.97\tau_c$). Fig. 10 represents the effective volume for test cascade radii in between 6 and 8.5 nm. The MD and the test effective volumes appear to follow a similar trend, which shows that Eq. (3) is in good agreement with the MD results. The test cascade radius that is consistent with the MD calculations lies in between 7 and 7.6 nm. This range will be compared in the following to the actual cascade radius.

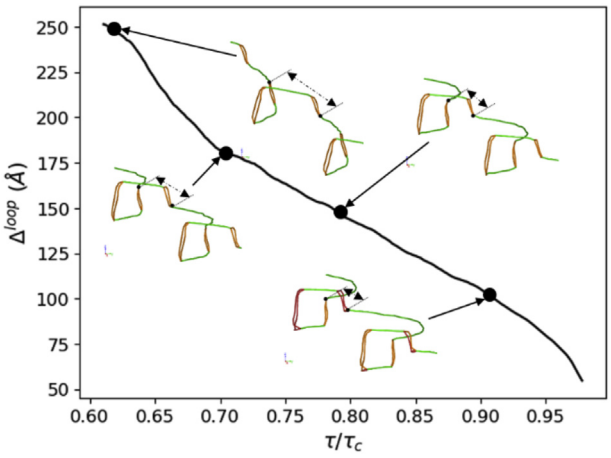

Fig. 9. Variation of the distance Δ^{loop} between the two pinning points during the contraction of the helical turn, the dislocation shape is displayed for different stress levels using the MD DXA module, the dislocation segments are displayed according to their type: the green and the orange segments are respectively in prismatic and basal planes. (For interpretation of the references to color in this figure legend, the reader is referred to the Web version of this article.)

4.3.2. Determination of the cascade radius using MD simulations

To determine the cascade radius, 10 MD calculations per PKA energy of single cascades without dislocations were performed for PKA energies of 5, 10, 15 and 20 keV. The irregular atoms were displayed using the adaptive Common Neighbor Analysis module of OVITO [36]. The convex-hull of these irregular atoms was then calculated. In Fig. 11a, a 10 keV cascade is displayed and its convex-hull is represented by black lines. The cascade radius R_c is calculated from the cascade volume V_c as $R_c = \sqrt[3]{3V_c/4\pi}$.

The results for the different PKA energies are represented in Fig. 12. Nonetheless, as shown in Fig. 11a, the convex-hull interior volume overestimates the cascade size and can be considered as an upper limit. To better fit the cascade shape, the "Construct surface mesh" [39] module of OVITO [36] was then used. After determining the convex-hull of the irregular atoms, this module removes parts of the convex-hull using a probe radius. The cascade radii

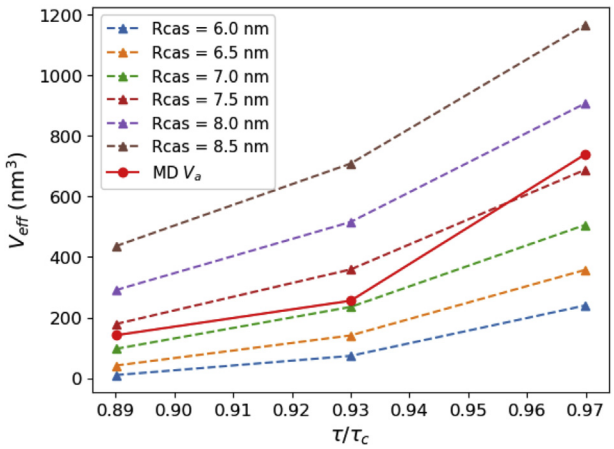

Fig. 10. Comparison of the effective volume obtained with the coarse mesh in MD with the test effective volume using different cascade radii for three stress levels.

corresponding to a probe radius r_p equal to the nearest neighbor atom separation ($r_p = 3.2$ Å) are represented in Fig. 12a. Nevertheless, as shown in Fig. 11a, some parts of the cascade are not included in the volume defined by the "Construct surface mesh" [39] module (in green), which suggests that the probe radius is too small. The cascade radius thus defined is a lower limit. The cascade size therefore lies in between the two extreme values obtained using the convex-hull of the cascade and the "Construct surface mesh" [39] module. Thus, for a cascade resulting from a 20 keV PKA, the cascade radius lies in a range between 5.6 nm and 8.0 nm, which includes the previously estimated test cascade radii consistent with the MD calculations.

Moreover, in order to check the influence of the PKA velocity direction, 15 calculations were performed with PKA velocity along four non-dense crystallographic directions ($[\bar{1}100]$, $[11\bar{2}1]$, $[02\bar{2}0]$ or $[\bar{1}101]$) with PKA energy of 20 keV. These simulations show that the size of the cascade does not depend on the initial PKA velocity direction, hence, within our model, neither does it affect the dislocation unpinning from the loop.

4.3.3. Determination of the cascade radius using the code Iradina [40]

Since it is time consuming to perform MD calculations for each PKA energy, the open source binary collision approximation (BCA) code Iradina [40] is used to estimate the cascades radii. The code Iradina allows the extraction of the interstitials and vacancies resulting from a cascade of a given PKA energy. Iradina is a code very similar to the frequently used SRIM code [40,41]. Calculations are performed on Iradina for 10 000 PKAs at 5, 10, 15 and 20 keV. The convex-hull of the vacancies and interstitials is then computed, and, as earlier, the cascade radius R_c was deduced from the volume of the convex-hull V_c. As shown in Fig. 12, the cascade mean radii for 5, 10, 15 and 20 keV are in the same ranges and lie between the two boundaries previously defined.

Moreover, for a 20 keV cascade, the cascade radius is equal to 7.0 nm, which is close to the test cascade radii consistent with the MD calculations (found between 7 and 7.5 nm). Thus, the Iradina cascade radii can be used as a valid first approximation of the actual cascades radii. Calculations are then performed on Iradina to estimate the cascade radii between 2 keV and 200 keV for 14 energy values. The values were linearly interpolated between the different energies. The results are presented in Fig. 12. Nonetheless, if the spherical approximation is roughly adequate for low energies PKA, there is a strong deviation from this approximation for high energy PKAs due to the formation of subcascades. This phenomenon will be discussed more in depth in section 5.

4.4. Summary of the methodology

The MD simulations have shown that the unpinning is more likely to occur when the cascade is generated in such a way as to encompass the pinning points of the dislocation and as the stress is getting larger. A closed-form model is developed in order to provide an estimate of the effective volume for a wide range of energies and loop characteristics. The model is based on the assumption that for the unpinning to occur, the cascade, considered to develop within a spherical volume, must encompass both pinning points of the dislocation.

Considering these simplifications, two parameters are needed to estimate the effective volume: the pinning point spacing $\Delta^{\text{loop}}(\tau)$, which depends on the stress level and on the loop characteristics, and the cascade radius $R_c(E_{\text{PKA}})$, which depends on the PKA energy.

For a given loop, a single MD calculation of the interaction of dislocation with the loop is needed to extract the pinning points spacing depending on the stress. The cascade radius for a given PKA energy can be estimated from quick BCA calculations using the code

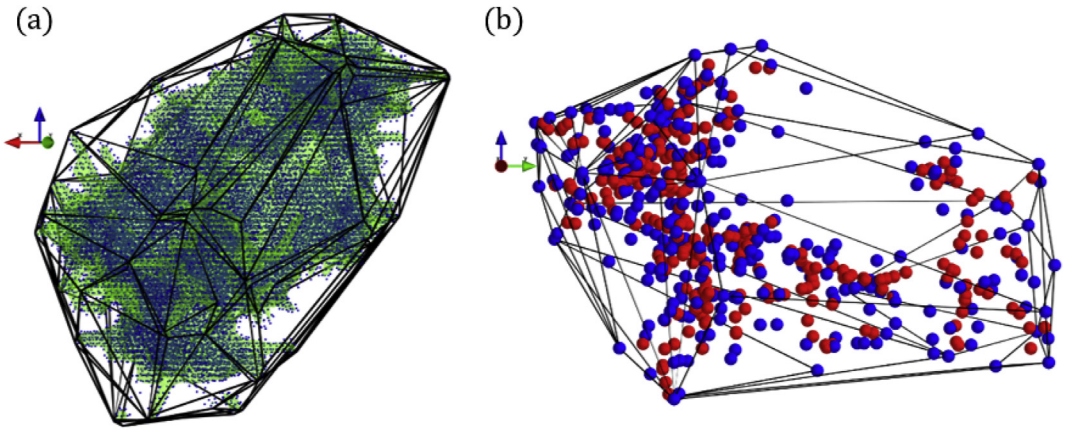

Fig. 11. (a) Cascade display at its peak of damage using the CNA module: the irregular atoms are displayed in blue, the green shape represents the cascade overlay using the MD "Construct Surface Mesh" module, the black lines represent the convex-hull of the cascade – (b) Vacancies (in red) and interstitials (in blue) obtained after the cascade relaxation using the Iradina software [40] and their convex-hull in black. (For interpretation of the references to color in this figure legend, the reader is referred to the Web version of this article.)

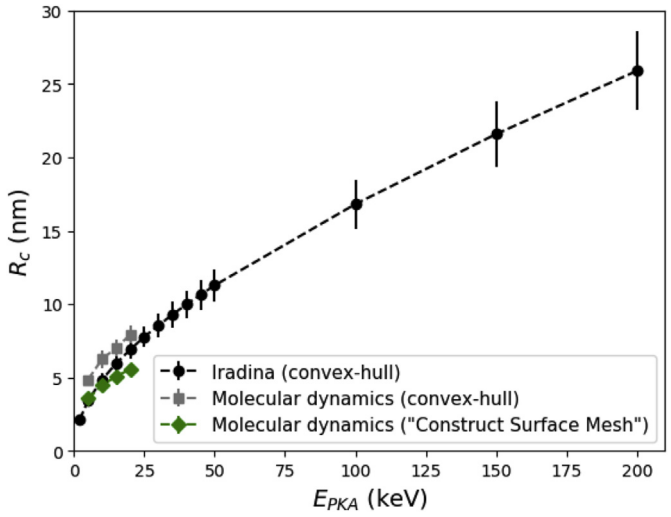

Fig. 12. Determination of the cascade radii as a function of the PKA energy: in green and grey using respectively the "Construct surface Mesh" module and the convex-hull method on the MD calculations, in black the convex-hull of the vacancies and interstitials obtained with the BCA code Iradina [40] after the relaxation of the cascade. (For interpretation of the references to color in this figure legend, the reader is referred to the Web version of this article.)

Iradina [40].

5. Comparison to ion and neutron irradiations

5.1. Comparison to the in situ experiments

Gaumé et al. [18] measured experimentally the mean pinning lifetime at room temperature for a "high" stress level (close to the critical stress). For each stress level, this lifetime can be expressed in terms of the number of "efficient" cascades around a given pinning point per unit of time $n_{\text{eff}}(\tau)$, for a given loop size and density, as

$$t_w(\tau) = \frac{1}{n_{\text{eff}}(\tau)} . \tag{4}$$

To estimate the number of "efficient" cascades, we have implemented a methodology similar to the one Kaoumi et al. developed to determine the average number of thermal spikes generated per ion [42]. A calculation is performed using the Monte Carlo code SRIM [43] in full cascade mode for $N_{\text{ions}} = 10\,000$ ions in the experimental conditions of Gaumé et al. [18]: 1 MeV Kr^+ for a specimen thickness of $e = 150$ nm. The PKA energy distribution predicted using SRIM is represented in Fig. 13. The loop characteristics in terms of size and density used in our MD calculations are assumed to be representative of the loops observed experimentally at room temperature. Every cascade (j) and the energy of the corresponding PKA (E^j_{PKA}) are recorded. However, high energy PKAs break up into subcascades, and we consider that cascades with energies E_{PKA} above a threshold energy E_{th} break up into $E_{\text{PKA}}/E_{\text{th}}$ spherical subcascades with an energy of E_{th}. De Backer et al. [44], combining BCA and MD calculations, suggest a threshold energy for zirconium of 40 keV. A lower value of 10 keV is suggested by Zhou et al. [45]. This value represents the transition between unfragmented cascades and cascades that are fragmented into both connected and unconnected cascades. However, in our model, we consider that the shape of a cascade fragmented into connected subcascades can be on average, as a first approximation,

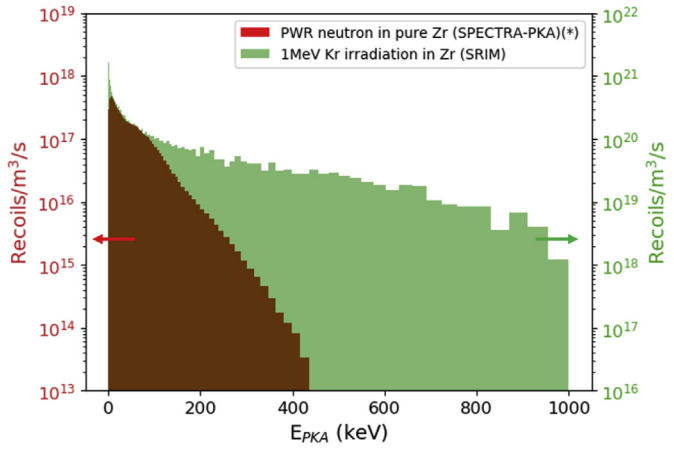

Fig. 13. Distribution of PKA energies predicted with the code SRIM in full calculation mode for 10 000 ions, and obtained with SPECTRA-PKA using a typical neutron flux spectrum. The data (*) are taken from Ref. [46].

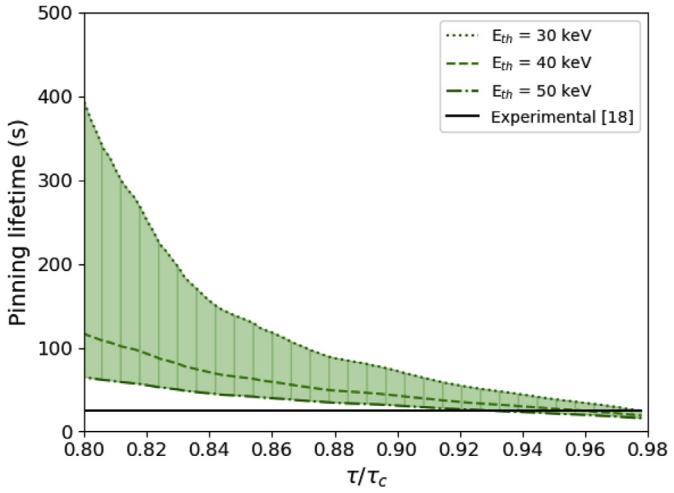

Fig. 14. Mean pinning lifetime evolution with stress obtained experimentally at high stress (solid line in black) [18], and with our model for a threshold energy E_{th} of 40 keV (dashed line in green), the hatched colored region represents the range of pinning point lifetimes for threshold energies in between 30 and 50 keV. (For interpretation of the references to color in this figure legend, the reader is referred to the Web version of this article.)

represented by one spherical cascade. This moves the threshold energy into higher values of around 40 keV based on Ref. [45]. Therefore, we have selected a threshold energy E_{th} of 40 keV.

For each cascade (j) generated in the SRIM calculation, we define a volume density per unit time ρ^j of similar cascades generated experimentally. Knowing the experimental ion flux ϕ and the specimen width e, ρ^j can be estimated according to

$$\rho^j = \frac{\phi}{N_{\text{ions}} \times e} . \tag{5}$$

Knowing the energy E^j_{PKA} of each cascade (j), the effective volume around the pinning point related to each cascade can be calculated at every stress level using expression (1). The number of "efficient" cascades for a given pinning point per unit time can then be expressed as follows

$$n_{\text{eff}}(\tau) = \sum_j \rho^j V_{\text{eff}}\left(\tau, E^j_{\text{PKA}}\right) = \frac{\phi}{N_{\text{ions}} \times e} \sum_j V_{\text{eff}}\left(\tau, E^j_{\text{PKA}}\right). \quad (6)$$

Since the experiments of Gaumé et al. [18] were performed at very high stress levels, the mean pinning point lifetime is calculated for stress levels above $0.8\tau_c$ using (2) and (4). Fig. 14 represents the variation of the mean pinning lifetime with increasing stress for a threshold energy E_{th} of 40 keV. To show the influence of the choice of the threshold energy, the range of pinning point lifetimes for threshold energies in between 30 keV and 50 keV are also represented. This figure illustrates that for high stress levels, the mean pinning point lifetime is of the same order of magnitude as in the experiments. It also shows that there is a great influence of the threshold energy chosen on the mean pinning lifetime, especially as the stress lowers.

The strain rate $\dot{\varepsilon}$ can be deduced from the mean pinning point lifetime, knowing the mean pinning point spacing L and the dislocation density ρ_d, using the following equation:

$$\dot{\varepsilon} = \rho_d b \frac{L}{t_w} \quad (7)$$

According to Eq. (4) and Eq. (6), $\dot{\varepsilon}$ is directly proportional to the flux. Fig. 15 represents the variation of $\dot{\varepsilon}/\phi$ as a function of the stress under the same conditions as in the experiments of Gaumé et al. [18] ($L = 1 \times 10^{-7}$ m and $\rho_d = 10^{11}$ m^{-2}), and taking a Burgers vector b of 3.23×10^{-10} m. However, it is important to note that the strain rate is estimated here assuming that the dependence of the mean pinning lifetime on the relative stress τ/τ_c obtained using our molecular dynamics simulation box can be extrapolated to a larger system.

For stresses above $0.8\tau_c$, the strain rate follows the law:

$$\dot{\varepsilon} = \alpha\phi\left(\frac{\tau}{\tau_c}\right)^{\beta} \quad (8)$$

where α is around 3.77×10^{-4} dpa^{-1} and β is of 8.33. In this equation, the flux ϕ is expressed in dpa/s. The high value of the stress exponent β is consistent with a high stress irradiation creep behavior.

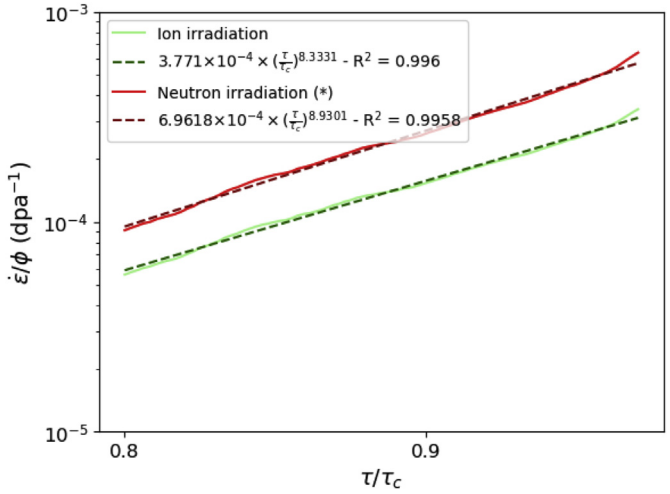

Fig. 15. Variation of the strain rate as a function of the stress for Kr ion irradiation and neutron irradiation. The input data for (*) are taken from Ref. [46].

5.2. Application to neutron irradiation

The methodology is now applied to neutrons in order to assess the relevance of the proposed mechanism in the case of neutron irradiation in-reactor. Adrych-Brunning et al. [47] calculated the PKA energy spectra for zirconium and zirconium alloys in PWRs using the software SPECTRA-PKA [48–50]. The outputs of the calculations for pure Zr using a typical PWR neutron flux spectrum [47,50] are freely available to download [46]. The PKA distribution thus obtained is represented in Fig. 13. Adrych-Brunning et al. [47] reported an average PKA energy of 6.9 keV, which is higher than the average PKA energy calculated using SRIM for the Kr irradiation, which is around 4 keV. This suggests that the PKAs generated during a neutron irradiation are more likely to be effective than the PKAs generated during an ion irradiation.

Table 2 represents, for four stress levels, the minimum PKA energy for which the unpinning is possible, and the proportion of PKAs that are effective in the case of ion irradiation and neutron irradiation. This evaluation is based on the raw data of SRIM and SPECTRA-PKA and takes into account the fragmentation of high-energy cascades into subcascades with a threshold energy of 40 keV using the method described above. This table shows that there are more effective PKAs in the case of a typical PWR neutron irradiation than a 1 MeV Kr irradiation, which is explained by the higher proportion of very low energy PKAs in the case of ions in comparison with neutrons, as it can be seen in Fig. 13.

The mean pinning lifetime can, again, be estimated knowing the number of recoils per volume per second ρ^i corresponding to the PKA energy E^i_{PKA}:

$$t_w(\tau) = \frac{1}{n_{\text{eff}}(\tau)} = \frac{1}{\sum_i \rho^i V_{\text{eff}}\left(\tau, E^i_{\text{PKA}}\right)} \quad (9)$$

The strain rate can then be estimated using Eq. (7). The evolution of $\dot{\varepsilon}/\phi$ with τ/τ_c, represented in Fig. 15, shows that the strain rate in the case of in-reactor neutron exposure condition also follows the law presented in Eq. (8), with a coefficient α around 6.96×10^{-4} dpa^{-1} and a coefficient β of 8.93. The coefficient β is very similar to the one obtained with ions and is consistent with high stress irradiation creep usual behavior. For stress levels ranging from $0.8\tau_c$ to $0.9\tau_c$, the ratio of the strain rate (in s^{-1}) divided by the damage rate (in dpa s^{-1}), $\dot{\varepsilon}/\phi$, ranges between 9.12×10^{-5} dpa^{-1} and 2.63×10^{-4} dpa^{-1}. The irradiation creep compliance for zirconium alloys is in the order of 10^{-6} up to 10^{-5} MPa^{-1} dpa^{-1} [5,51,52]. Thus, for a stress around 100 MPa, $\dot{\varepsilon}/\phi$ is around 10^{-4} up to 10^{-3} dpa^{-1}. Therefore, the values obtained for $\dot{\varepsilon}/\phi$ using our model are not negligible compared with the strain rates measured in reactor, and the mechanism proposed may be relevant to explain irradiation creep deformation at high stress levels.

6. Conclusions

A mechanism of irradiation creep at high stress levels was proposed by Gaumé et al. for zirconium alloys [18]: a dislocation pinned on an irradiation defect can be released by a displacement cascade occurring in an effective volume around the pinning points of the dislocation. Here, we performed numerous MD simulations in α-zirconium to investigate statistically the effect of 20 keV displacement cascades on a screw dislocation pinned on an interstitial loop at different stress levels.

The main findings of this work are:

Table 2
Minimum energy for an effective PKA and proportion of effective PKAs for ion and neutron irradiation for four stress levels. The data (*) are extracted from [46].

Stress level	$0.8\tau_c$	$0.85\tau_c$	$0.9\tau_c$	$0.95\tau_c$
E_{PKA}^{min} (keV)	21.5	16.1	11.8	6.7
Proportion of effective PKAs - Kr irradiation	7.65%	8.41%	9.37%	11.59%
Proportion of effective PKAs - neutron irradiation (*)	11.51%	13.85%	17.17%	23.91%

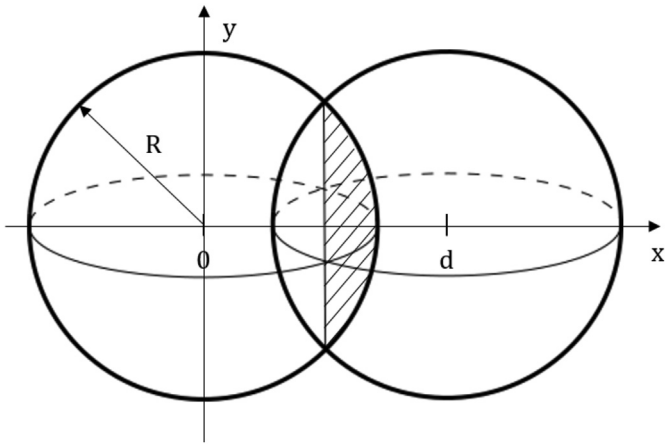

Fig. 16. Intersection between two spheres of equal radius.

- A direct unpinning by displacement cascades of a dislocation pinned on an interstitial loop is observed at high stress levels in the MD simulations (for stress levels equal to $0.86\tau_c$, $0.89\tau_c$, $0.93\tau_c$ and $0.97\tau_c$);
- The dislocation unpinning seems to occur when the displacement cascade encompasses the two pinning points of the dislocation;
- The effective volume expands with increasing stress, which is in good agreement with the experimental observations of Gaumé et al. [18];
- A simple closed-form model is proposed: the unpinning occurs when the cascade, assumed spherical, intercepts both pinning points of the dislocation. The determination of the effective volume is thus reduced to simple geometrical considerations depending on two parameters only: the cascade radius, which can be deduced from BCA calculations performed on Iradina [40], and the distance between the pinning points, which can be determined from a single MD simulation;
- The effective volumes calculated at different stress levels using this simple model are in good agreement with the one estimated from the MD simulations of cascades on pinned dislocation;
- The mean pinning point lifetime in the experimental conditions of Gaumé et al. [18] is estimated using this model and is found in the same order of magnitude for high stress levels as in the experiments, indicating that the unpinning mechanism proposed can explain the stop-and-go dislocation motion observed experimentally;
- When applied to a usual PWR neutron irradiation of pure zirconium, the proportion of effective PKAs is predicted to be higher for a neutron irradiation than for a Kr ion irradiation.
- Both for Kr ion and PWR neutron irradiation, the strain rate follows a creep law $\dot{\varepsilon} = \alpha\phi(\tau/\tau_c)^{\beta}$, with a high stress exponent β of 8.33 for a Kr ion irradiation, and 8.93 for a usual PWR neutron irradiation of zirconium, which is compatible with a high stress irradiation creep behavior. The strain rates predicted for PWR neutrons can be significant and can provide a valid explanation for high stress irradiation creep.

Data availability

The raw/processed data required to reproduce these findings cannot be shared at this time due to technical or time limitations.

CRediT authorship contribution statement

Nargisse Khiara: Methodology, Investigation, Writing - original draft, Visualization, Formal analysis. **Fabien Onimus:** Conceptualization, Methodology, Writing - original draft, Supervision, Funding acquisition. **Laurent Dupuy:** Conceptualization, Methodology, Software. **Wassim Kassem:** Software, Data curation. **Jean-Paul Crocombette:** Conceptualization, Methodology, Software, Writing - review & editing, Formal analysis. **Thomas Pardoen:** Conceptualization, Supervision, Writing - review & editing. **Jean-Pierre Raskin:** Conceptualization, Supervision. **Yves Bréchet:** Conceptualization, Supervision.

Declaration of competing interest

The authors declare that they have no known competing financial interests or personal relationships that could have appeared to influence the work reported in this paper.

Appendix

The intersection of two spheres of equal radius R centered on (0, 0, 0) and $(d, 0, 0)$ is a circle lying in the (yz) plane at $x = d/2$ with a radius a defined as follows:

$$a = \frac{1}{2}\sqrt{4R^2 - d^2}$$

The volume V of the three-dimensional lens common to the two spheres can be calculated by adding the volume of the two spherical caps of height $R - \frac{d}{2}$ (dashed volume represented in Fig. 16).

Moreover, the volume V_0 of a spherical cap of height h for a sphere of radius R is defined by:

$$V_0 = \frac{\pi h^2}{3}(3R - h)$$

Thus, the volume of the lens at the intersection of the two spheres is (with $h = R - \frac{d}{2}$):

$$V = 2V_0 = \frac{\pi}{12}(2R - d)^2(4R + d)$$

Appendix B. Supplementary data

Supplementary data related to this article can be found at https://doi.org/10.1016/j.jnucmat.2020.152336.

References

[1] C. Lemaignan, in: R. Konings (Ed.), Zirconium Alloys: Properties and Characteristics, Comprehensive Nuclear Materials, vol. 2, Elsevier Ltd., Oxford, 2012, pp. 217–232.
[2] D.G. Franklin, R.B. Adamson, Implications of Zircaloy creep and growth to light water reactor performance, J. Nucl. Mater. 159 (1988) 12–21.
[3] M. Griffiths, A review of microstructure evolution in zirconium alloys during irradiation, J. Nucl. Mater. 159 (1988) 190–218.
[4] R.A. Holt, In-reactor deformation of cold-worked Zr–2.5 Nb pressure tubes, J. Nucl. Mater. 372 (2-3) (2008) 182–214.
[5] F. Onimus, J.L. Béchade, in: R. Konings (Ed.), Radiation Effects in Zirconium Alloys, Comprehensive Nuclear Materials, vol. 4, Elsevier Ltd., Oxford, 2012, pp. 1–31.
[6] D.G. Franklin, G.E. Lucas, A.L. Bement, Creep of zirconium alloys in nuclear reactors 815, ASTM STP, 1983.
[7] R.B. Adamson, C.E. Coleman, M. Griffiths, Irradiation creep and growth of zirconium alloys: a critical review, J. Nucl. Mater. 521 (2019) 167–244.
[8] G.W. Lewthwaite, D. Mosedale, I.R. Ward, Irradiation creep in several metals and alloys at 100 C, Nature 216 (5114) (1967) 472.
[9] R. Taylor, A.T. Jeffs, The effect of irradiation on stress relaxation in Nimonic 80A, J. Nucl. Mater. 19 (2) (1966) 142–148.
[10] D. Mosedale, Influence of irradiation on creep, J. Appl. Phys. 33 (10) (1962) 3142–3143.
[11] V. Fidleris, Uniaxial in-reactor creep of zirconium alloys, J. Nucl. Mater. 26 (1) (1968) 51–76.
[12] V. Fidleris, The irradiation creep and growth phenomena, J. Nucl. Mater. 159 (1988) 22–42.
[13] F.A. Nichols, On the mechanisms of irradiation creep in zirconium-base alloys, J. Nucl. Mater. 37 (1) (1970) 59–70.
[14] J. Gittus, Creep, Viscoelasticity and Creep Fracture in Solids, vol. 16, Applied Science Publishers, London, 1975.
[15] L.K. Mansur, Irradiation creep by climb-enabled glide of dislocations resulting from preferred absorption of point defects, Philos. Mag. A 39 (4) (1979) 497–506.
[16] J.R. Matthews, M.W. Finnis, Irradiation creep models—an overview, J. Nucl. Mater. 159 (1988) 257–285.
[17] F.A. Garner, D.S. Gelles, Irradiation creep mechanisms: an experimental perspective, J. Nucl. Mater. 159 (1988) 286–309.
[18] M. Gaumé, P. Baldo, F. Mompiou, F. Onimus, In-situ observation of an irradiation creep deformation mechanism in zirconium alloys, Scripta Mater. 154 (2018) 87–91.
[19] B.T. Kelly, A.J.E. Foreman, The theory of irradiation creep in reactor graphite—the dislocation pinning-unpinning model, Carbon 12 (2) (1974) 151–158.
[20] S.J. Wooding, L.M. Howe, F. Gao, A.F. Calder, D.J. Bacon, A molecular dynamics study of high-energy displacement cascades in α-zirconium, J. Nucl. Mater. 254 (2-3) (1998) 191–204.
[21] C. Dai, L. Balogh, Z. Yao, M.R. Daymond, The habit plane of ⟨a⟩-type dislocation loops in α-zirconium: an atomistic study, Phil. Mag. 97 (12) (2017) 944–956.
[22] R.E. Voskoboinikov, Y.N. Osetsky, D.J. Bacon, Statistics of primary damage creation in high-energy displacement cascades in copper and zirconium, Nucl. Instrum. Methods Phys. Res. Sect. B Beam Interact. Mater. Atoms 242 (1-2) (2006) 68–70.
[23] F. Gao, D.J. Bacon, L.M. Howe, C.B. So, Temperature-dependence of defect creation and clustering by displacement cascades in α-zirconium, J. Nucl. Mater. 294 (3) (2001) 288–298.
[24] S. Di, Z. Yao, M.R. Daymond, F. Gao, Molecular dynamics simulations of irradiation cascades in alpha-zirconium under macroscopic strain, Nucl. Instrum. Methods Phys. Res. Sect. B Beam Interact. Mater. Atoms 303 (2013) 95–99.
[25] W. Zhou, J. Tian, J. Zheng, J. Xue, S. Peng, Dislocation-enhanced experimental-scale vacancy loop formation in hcp Zirconium in one single collision cascade, Sci. Rep. 6 (2016) 21034.
[26] R.E. Voskoboynikov, Y.N. Osetsky, D.J. Bacon, Self-interstitial atom clusters as obstacles to glide of 1/3< 11-20>{1-100} edge dislocations in α-zirconium, Mater. Sci. Eng., A 400 (2005) 54–58.
[27] A. Serra, D.J. Bacon, Atomic-level computer simulation of the interaction between dislocations and interstitial loops in α-zirconium, Model. Simulat. Mater. Sci. Eng. 21 (4) (2013), 045007.
[28] K. Ghavam, R. Gracie, Simulations of reactions between irradiation induced< a>-loops and mixed dislocation lines in zirconium, J. Nucl. Mater. 462 (2015) 126–134.
[29] S. Plimpton, Fast parallel algorithms for short-range molecular dynamics, J. Comput. Phys. 117 (1995) 1–19. http://lammps.sandia.gov.
[30] M. Mendelev, G. Ackland, Development of an interatomic potential for the simulation of phase transformations in zirconium, Phil. Mag. Lett. 87 (2007) 349–359.
[31] H.A. Khater, D.J. Bacon, Dislocation core structure and dynamics in two atomic models of α-zirconium, Acta Mater. 58 (8) (2010) 2978–2987.
[32] N. De Diego, A. Serra, D.J. Bacon, Y.N. Osetsky, On the structure and mobility of point defect clusters in alpha-zirconium: a comparison for two interatomic potential models, Model. Simulat. Mater. Sci. Eng. 19 (3) (2011), 035003.
[33] S. Di, Z. Yao, M.R. Daymond, X. Zu, S. Peng, F. Gao, Dislocation-accelerated void formation under irradiation in zirconium, Acta Mater. 82 (2015) 94–99.
[34] D.J. Bacon, Y. Osetsky, R. Rodney, Dislocation–obstacle interactions at the atomic level, in: Dislocations in Solids, vol. 15, 2009, pp. 1–90.
[35] M.S. Daw, S.M. Foiles, M.I. Baskes, The embedded-atom method: a review of theory and applications, Mater. Sci. Rep. 9 (7-8) (1993) 251–310.
[36] A. Stukowski, Visualization and analysis of atomistic simulation data with OVITO–the Open Visualization Tool, Model. Simulat. Mater. Sci. Eng. 18 (1) (2009), 015012.
[37] J.D. Honeycutt, H.C. Andersen, Molecular dynamics study of melting and freezing of small Lennard-Jones clusters, J. Phys. Chem. 91 (19) (1987) 4950–4963.
[38] A. Stukowski, K. Albe, Extracting dislocations and non-dislocation crystal defects from atomistic simulation data, Model. Simulat. Mater. Sci. Eng. 18 (8) (2010), 085001.
[39] A. Stukowski, Computational analysis methods in atomistic modeling of crystals, JOM (J. Occup. Med.) 66 (3) (2014) 399–407.
[40] C. Borschel, C. Ronning, Ion beam irradiation of nanostructures - a 3D Monte Carlo simulation code, Nucl. Instrum. Methods Phys. Res. Sect. B Beam Interact. Mater. Atoms 269 (2011) 2133–2138.
[41] J.P. Crocombette, C. Wambeke, Quick calculation of damage for ion irradiation: implementation in Iradina and comparisons to SRIM, EPJ Nucl Sci. Technol. 5 (2019).
[42] D. Kaoumi, A.T. Motta, R.C. Birtcher, A thermal spike model of grain growth under irradiation, J. Appl. Phys. 104 (7) (2008), 073525.
[43] J.F. Ziegler, J.P. Biersack, U. Littmark, The Stopping and Range of Ions in Solids, Pergamon, New York, 1985 [Online]. Available: http://www.srim.org/.
[44] A. De Backer, A.E. Sand, K. Nordlund, L. Luneville, D. Simeone, S.L. Dudarev, Subcascade formation and defect cluster size scaling in high-energy collision events in metals, EPL (Europhys Lett) 115 (2) (2016) 26001.
[45] W. Zhou, J. Tian, Q. Feng, J. Zheng, X. Liu, J. Xue, D. Qian, S. Peng, Molecular dynamics simulations of high-energy displacement cascades in hcp-Zr, J. Nucl. Mater. 508 (2018) 540–545.
[46] M. Gilbert, SPECTRA-PKA, SPECTRA-PKA is available as a utility within FISPACT-II, and now also, available to download from github at, https://github.com/fispact/SPECTRA-PKA, 2018.
[47] A. Adrych-Brunning, M.R. Gilbert, J.C. Sublet, A. Harte, C.P. Race, Modelling the interaction of primary irradiation damage and precipitates: implications for experimental irradiation of zirconium alloys, J. Nucl. Mater. 498 (2018) 282–289.
[48] M.R. Gilbert, J. Marian, J.C. Sublet, Energy spectra of primary knock-on atoms under neutron irradiation, J. Nucl. Mater. 467 (2015) 121–134.
[49] J.C. Sublet, J.W. Eastwood, J.G. Morgan, M.R. Gilbert, M. Fleming, W. Arter, FISPACT-II: an advanced simulation system for activation, transmutation and material modelling, Nucl. Data Sheets 139 (2017) 77–137.
[50] J.C. Sublet, J.W. Eastwood, J.G. Morgan, M. Fleming, M.R. Gilbert, Technical report UKAEA-R(11)11, in: FISPACT-II User Manual, vol. 8, UK Atomic Energy Authority, 2016.
[51] F. Onimus, T. Jourdan, C. Xu, A. Campbell and M. Griffiths, "Irradiation creep in materials," in Comprehensive Nuclear Materials, R. Konings ed., Elsevier Ltd., Oxford, To (be published).
[52] P.A. Turner, C.N. Tomé, N. Christodoulou, C.H. Woo, A self-consistent model for polycrystals undergoing simultaneous irradiation and thermal creep, Philos. Mag. A 79 (10) (1999) 2505–2524.